



Regular Article

Antimicrobial peptide induced colloidal transformations in bacteria-mimetic vesicles: Combining in silico tools and experimental methods



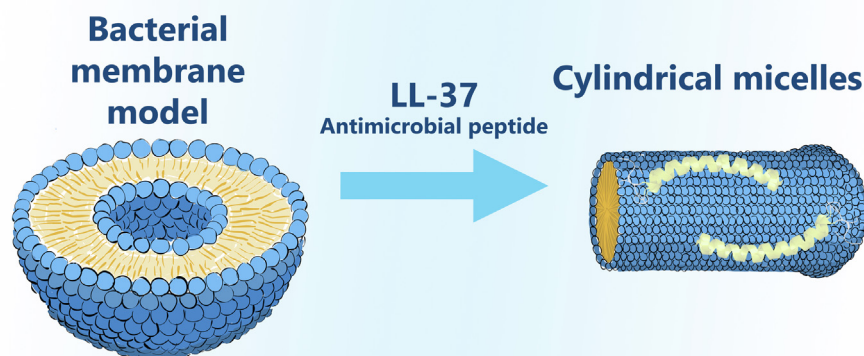
Rafael V.M. Freire^a, Yeny Pillco-Valencia^b, Gabriel C.A. da Hora^{b,1}, Madeleine Ramstedt^c, Linda Sandblad^c, Thereza A. Soares^{b,*}, Stefan Salentinig^{a,*}

^a Department of Chemistry, University of Fribourg, Chemin Du Musée 9, 1700 Fribourg, Switzerland

^b Department of Fundamental Chemistry, Federal University of Pernambuco, Cidade Universitária, 50740-560 Recife, Brazil

^c Department of Chemistry, Umeå Center for Microbial Research, Umeå University, SE-901 87 Umeå, Sweden

GRAPHICAL ABSTRACT



ARTICLE INFO

Article history:

Received 30 December 2020

Revised 9 March 2021

Accepted 11 March 2021

Available online 16 March 2021

Keywords:

Vesicles

Antimicrobial peptides

POPG

LL-37

Self-assembly

SAXS

Cryo-TEM

Coarse-grain molecular dynamics simulations

ABSTRACT

With the growing challenges of bacteria becoming resistant to conventional antibiotics, antimicrobial peptides (AMPs) may offer a potential alternative. One of the most studied AMPs, the human cathelicidin derived AMP LL-37 is notable for its antimicrobial activity even though its mechanism of action is not fully understood yet. This work investigates the interaction of LL-37 with 1-Palmitoyl-2-oleoyl-*sn*-glycero-3-phospho-rac-(1-glycerol) (POPG) vesicles, which were employed as a bacterial membrane model given the common presence of this phospholipid in the bacterial membrane. Experimental techniques including small angle X-ray scattering, transmission electron microscopy and dynamic light scattering were used to characterize the interactions among LL-37 and POPG. Molecular dynamics simulations complement the experimental studies with molecular-level insights into the process. LL-37 was discovered to actively and critically interact with the POPG vesicles, modifying the membrane curvature that eventually leads to structural transformations from vesicles to mixed micelles. The results shed light on the mechanisms underlying the interactions among LL-37 and bacteria mimetic vesicles and can guide the further development of AMP based antimicrobial materials and therapies.

© 2021 The Authors. Published by Elsevier Inc. This is an open access article under the CC BY license (<http://creativecommons.org/licenses/by/4.0/>).

* Corresponding authors.

E-mail address: stefan.salentinig@unifr.ch (S. Salentinig).

¹ Present address: Department of Chemistry, University of Utah, Salt Lake City 84112, United States.

1. Introduction

Antimicrobial resistance has become a global health threat [1]. Antimicrobial peptides (AMPs) are a potential alternative to combat bacteria that are resistant to conventional antibiotics. AMPs are key components of the innate immune system in all known living organisms [2]. Their major advantages over conventional antibiotics are the much lower rate of acquired resistance, the lower induction of bacterial mutagenesis and the possibility of usage by immunocompromised individuals [3–6]. In addition to the antibacterial properties, AMPs can also display antiviral, antifungal and anticancer properties [7–9]. Some AMPs were reported to increase cell proliferation and activate the innate and adaptive immunity mechanisms [10–12]. The main feature that enables AMPs to have antimicrobial activity is their ability to penetrate and disrupt the cellular membranes of bacteria [13]. The positive charge of AMPs contributes to the selectivity for the mostly negatively charged bacterial cells rather than mammalian cells [14]. However, the detailed mechanisms at play on the molecular and colloidal scale are not yet fully understood. There are yet a few challenges to overcome for the therapeutic usage of AMPs such as the development of efficient delivery systems capable of protecting the AMPs from biological degradation and reducing their side effects by means of targeted release [15,16].

LL-37 is the only AMP of the cathelicidin family found in humans [17]. It contains 37 amino acids, with 16 of them being charged and hydrophilic. Out of these 16 hydrophilic residues, 5 are negatively charged and 11 are positively charged, leading to an overall charge of +6 at pH 7 [18,19]. The coexistence of both negative and positive groups in AMPs is very important to the destabilization of the packing of lipid bilayers [20]. Regarding its secondary structure, LL-37 belongs to the α -helical class of AMPs, possessing one face of the helix with a hydrophobic character while the opposite side has a hydrophilic character [21].

Bacterial cell membranes have a considerable number of anionic phospholipids such as phosphatidylglycerol (PG) while mammalian cell membranes are mainly composed of zwitterionic phospholipids such as phosphatidylcholine (PC), which results in bacterial cell surfaces possessing typically negative charge whereas mammalian cell surfaces have a more neutral character [22,23]. 1-Palmitoyl-2-oleoyl-*sn*-glycero-3-phospho-rac-(1-glycerol) (POPG) bilayers have been employed as a bacterial membrane model for studies involving AMPs [24–28] based on its chain-length, charge and capacity to form vesicles in water.

Unraveling the mechanisms of action of AMPs involving lipid phase change and formation of peptide-lipid nanostructures are gaining more attention recently [29–31]. Due to their amphiphilic nature, AMPs can form intermolecular interactions with both the polar head group and the hydrophobic tail of lipids. These interactions can induce colloidal transformations on the bacterial membranes, which can be linked to the antimicrobial activity of AMPs. Therefore, it is of great importance to develop a deeper understanding of these mechanisms in order to boost the efficacy of AMP-based therapies. Models based on amphiphilic lipids - such as vesicles, supported monolayers and supported lipid bilayers - have been used to mimic the bacteria membrane and study the interaction with AMPs [32,33]. For the particular case of LL-37, its interaction with membranes is not fully understood and this has been the target of many studies using a variety of membrane models and characterization techniques. While some studies point towards a toroidal pore formation [34–36], others suggest a carpet-like mode of action [37–40]. The formation of supramolecular fiber-like structures of LL-37 on the bacterial surface was also discussed as a reason for its antimicrobial activity [41]. Another potential mechanism relies on the acceleration of flip-flop motion

and the molecular transport of phospholipids without changes of the overall membrane structure [42].

Techniques such as small angle X-ray scattering (SAXS) and cryogenic electron microscopy (cryo-EM) have provided valuable information on the colloidal interactions of AMPs with membrane-mimetic lipid systems [43,44]. Combining these techniques with molecular dynamics allows for a molecular-level visualization of the colloidal transformations, providing valuable information on the colloidal transformations that drive AMP activity. As a surface-active peptide, LL-37 is capable of affecting the self-assembly of different polar lipids. For example, the addition of LL-37 to glycerol monooleate (GMO) based cubosomes revealed the composition-dependent transformation from cubosomes to lamellar and micellar structures [45,46]. LL-37 induced colloidal transformations were also reported for the oleic acid (OA) based self-assembled structures [47,48]. However, further knowledge on the mechanisms underlying LL-37 induced membrane destabilization on the molecular and colloidal length-scales is required for a detailed understanding of the antimicrobial activity and the rational design of novel antimicrobial systems.

In this study, SAXS, cryo-EM and dynamic light scattering (DLS), together with coarse grain molecular dynamics (CG MD) simulations are used to investigate the effect of LL-37 addition to POPG vesicles on the molecular and colloidal scales. With increasing LL-37 concentration, a gradual transformation from POPG vesicles to cylindrical POPG / LL-37 micelles were discovered. Consistently, CG MD simulations show that in presence of high concentration of LL-37, POPG bilayers spontaneously transform into flat micelles. The picture emerging from these findings cannot be easily conciliated with a presumed pore formation mechanism for LL37 in POPG vesicles.

2. Materials and methods

2.1. Vesicle preparation

60 mg of POPG sodium salt (Avanti Polar Lipids, Inc., purity > 99%, Darmstadt, Germany) was dissolved in 0.5 mL of chloroform (Sigma-Aldrich, >99%, Buchs, Switzerland) and the solution was vacuum evaporated in a 10 mL round flask overnight using a rotary evaporator (Büchi R-134, Switzerland). The formed lipid film was suspended in phosphate-buffered saline (PBS, 10 mM, pH 7.4), at a concentration of 2% (w/w). The suspension was sonicated using an ultrasonic probe-type sonicator (Sonics VibraCell VCX 130 W, 20 kHz, Sonics & Materials Inc., Newton, CT, USA) with 1 min at 20% of the maximum power of 130 W (1 s pulsing, 1 s break) followed by 2 min at 27% of maximum power (3 s pulsing, 5 s break). 12.5 mg of LL-37 peptide (98.3% purity, Bachem AG, Bubendorf, Switzerland) was dissolved in PBS buffer (10 mM, pH 7.4) at a concentration of 2% (w/w) and then combined with the POPG vesicle solution at various mass ratios (namely POPG/LL-37 4:1, 3:1, 2.5:1, 2:1, 1.5:1, 1:1 and 1:2). Then the samples were equilibrated for one hour at room temperature and characterized.

2.2. Dynamic light scattering (DLS) and zeta-potential measurements

DLS and zeta potential measurements were performed on a Malvern Zetasizer Nano ZS90 (633 nm He-Ne Laser, Malvern Instruments, USA). Samples were diluted 10 times with PBS buffer at pH 7.4 and centrifuged at 1000g for 10 min to remove any dust and air bubbles (Centrifuge Eppendorf 5417-R, Germany). DLS measurements were done in triplicate at 25 °C on glass cells with optical path of 10 mm. For zeta potential measurements, samples were measured on DTS1070 capillary cells (Malvern Instruments Ltd., U.K.). The cumulant method was used to calculate the appar-

ent hydrodynamic diameter and the polydispersity index (PDI) [49,50].

2.3. Small angle X-ray scattering (SAXS)

Small angle X-ray scattering measurements were carried out on a Bruker Nanostar U (Bruker AXS, Karlsruhe, Germany) with a sealed-tube Cu anode source at 50 kV and 600 μ A (Incoatec I μ SCu, Geest-hacht, Germany). The X-ray beam was filtered by a Göbel mirror into a monochromatic Cu K α radiation (wavelength 1.5406 Å). The detector (VANTEC-2000, Bruker AXS, Karlsruhe, Germany) had an active area of 140 \times 140 mm² and pixel size of 68 μ m. The data collected at the detector were azimuthally integrated into one-dimensional scattering curves $I(q)$, where q is the length of the scattering vector, defined by $q = 4\pi / \lambda \sin(\theta/2)$, λ is the wavelength and θ is the scattering angle. Exposure time was set to 60 min for each sample; and sample to detector distance was 1.05 m, providing a q -range $0.008 < q < 0.29 \text{ Å}^{-1}$. Glassy carbon was measured with all samples for transmittance corrections, relative to the transmittance of the buffer (background). The PBS buffer scattering curve was subtracted as background from all samples. Measurements were carried out at room temperature (25 °C) in thin-walled glass capillaries with outside diameter of 1.5 mm (Hilgenberg GmbH, Malsfeld, Germany).

2.4. SAXS data analysis

2.4.1. Model-independent SAXS fitting

Vesicles and micelles were identified by their characteristic power-law scattering at low q values [51]. The generalized indirect Fourier transformation method (GIFT) was used to further analyse the vesicles and micelles. The calculated pair-distance distribution functions $p(r)$ provide information on the size, shape and morphology of the scattering objects [52]. This method can separate the scattering intensity contributions of N number of monodisperse, homogenous, and spherical particles into the form factor $P(q)$, and the structure factor $S(q)$ with

$$I(q) = NS(q)P(q) \quad (1)$$

The $S(q)$ could be well approximated with 1 (absence of structure factor) for the selected systems, resulting in reasonable $p(r)$ functions and fits to the $I(q)$; except for multilamellar POPG vesicles where a structure factor peak was visible in the SAXS data. In this case, the structure factor was obtained with a lamellar model (Modified Caillé Theory [53]). Optimization was carried out through Boltzmann simplex simulated annealing [54]. The $p(r)$ is linked to the form factor $P(q)$ by equation (2):

$$P(q) = 4\pi \int_0^\infty p(r) \frac{\sin qr}{qr} dr \quad (2)$$

For particles of arbitrary shape, the $p(r)$ is given by $p(r) = r^2 \Delta \rho^2(r)$ where $\Delta \rho^2(r)$ is the convolution square of the excess electron density distribution, $\Delta \rho(r)$, averaged over all directions in the space. In order to extract $\Delta \rho(r)$ from $p(r)$, a deconvolution procedure can be carried out, with prior assumption of the symmetry of the system (spherical, lamellar or cylindrical) [55]. The thickness of the bilayer is very small compared to the vesicle diameter, which allows the assumption of locally flat lamellar structures for evaluation and the calculation of a thickness pair-distance distribution function, $p_t(r)$. [56] In the case of cylindrical micelles with a sufficient length/diameter ratio (>3), the cross section of the cylinders can be investigated using the cross-section pair distance distribution function, $p_c(r)$. The deconvolution of the $p_t(r)$ and $p_c(r)$ gives the thickness- or cross-sectional contrast profile in electron density $\Delta \rho_t$ and $\Delta \rho_c$, respectively. [56] These

excess electron density profiles (relative to the PBS buffer) give information about the internal structure of the scattering objects. Most vesicles and cylindrical micelles have a core-shell-type structure, with a hydrophobic core with the alkyl chains of the POPG, and the hydrophilic shell also containing counterions and bound solvent molecules. If there is a difference in the excess electron density, the radius of the core and the thickness of the shell can be discerned directly from the radial contrast profile.

In the presence of Bragg reflections, the inter-lamellar distance d for multilamellar vesicles can also be calculated using

$$d = \frac{2\pi h}{q_h} \quad (3)$$

where h is the order of the Bragg peak, and q_h is the q -value of the h -th order Bragg peak.

2.4.2. Model-dependent analysis

Model-dependent fitting of the scattering data (form factor scattering) was used to gain insights into nanostructure and morphology of the self-assemblies.

In case of vesicles, following equation was used [57]

$$I(q) = 2\pi \frac{\text{scalefactor}}{2(\delta_H + \delta_T)} P(q) \frac{1}{q^2} + \text{background} \quad (4)$$

with

$$P(q) = \frac{4}{q^2} \{ \Delta \rho_H [\sin(q\delta_H + \delta_T)] - \sin(q\delta_T) \} + \Delta \rho_T \sin(q\delta_T) \}^2 \quad (5)$$

where δ_H is the length of the head group, δ_T is the length of the tail group, $P(q)$ is the form factor, $\Delta \rho_H$ is the difference between the electron densities of head group and solvent and $\Delta \rho_T$ is the difference between the electron densities of tail group and solvent.

For core-shell cylinders, following equations were used to calculate the best possible fit to the experimental data [58]:

$$I(q, \alpha) = \frac{\text{scalefactor}}{V_s} F^2(q, \alpha) \sin(\alpha) + \text{background} \quad (6)$$

with

$$F(q, \alpha) = (\rho_{\text{tail}} - \rho_{\text{head}}) V_c \frac{\sin(q \frac{1}{2} L \cos(\alpha))}{q \frac{1}{2} L \cos(\alpha)} \frac{2J_1(qR \sin(\alpha))}{qR \sin(\alpha)} + (\rho_{\text{head}} - \rho_{\text{solvent}}) V_s \frac{\sin(q(\frac{1}{2}L + T) \cos(\alpha))}{q(\frac{1}{2}L + T) \cos(\alpha)} \times \frac{2J_1(q(R + T) \sin(\alpha))}{q(R + T) \sin(\alpha)} \quad (7)$$

$$V_s = \pi(R + T)^2(L + 2T) \quad (8)$$

and

$$V_c = \pi R^2 L \quad (9)$$

Here α is the cylinder axis angle in relation to scattering vector magnitude q , V_s is the total volume, V_c is the core volume, L is the length of the core, R is the radius of the core, T is the thickness of the shell, ρ_{tail} is the electron density of the core (lipid tail), ρ_{head} is the electron density of the shell (lipid headgroup), ρ_{solvent} that of the solvent, J_1 is a Bessel function of first order. The model is corrected for random orientation by the equation (Eq. (10)):

$$F^2(q) = \int_0^{\frac{\pi}{2}} F^2(q, \alpha) \sin(\alpha) d\alpha \quad (10)$$

Initially, the model only accounts for cylinders at a single orientation angle. When the cylinders are randomly orientated, then it is necessary to integrate $F^2(q, \alpha) \sin(\alpha)$ over all possible angles (from

Table 1Simulated systems. CG MD simulations of POPG mixtures (Sys_M) and bilayers (Sys_B) in presence of increasing concentrations of the LL-37 peptide.

System	Number of Molecules				Mass Ratio POPG/LL-37
	LL-37	Lipids	Water	Ions	
Sys _M -1	–	600	5574	912	–
Sys _M -2	5	600	54,418	2016	21:1
Sys _M -3*	5	600	54,418	2016	21:1
Sys _M -4	80	4160	181,728	8732	4:1
Sys _B -1	–	520	5207	114	–
Sys _B -2	–	520	4800	520	–
Sys _B -3	8	520	13,742	568	11:1
Sys _B -4	40	2080	78,394	2320	9:1
Sys _B -5*	40	2080	87,835	2320	9:1
Sys _B -6	60	2080	110,289	2440	6:1
Sys _B -7	40	600	51,796	1806	3:1

* Simulations performed using anisotropic pressure coupling.

0 to 90° due to symmetry) and thus it is possible to replace $F^2(q, \alpha) \sin(\alpha)$ by $F^2(q)$ in Eq. (6).

In case of mixtures between vesicles and cylindrical micelles, the experimental SAXS curves were approximated using a composite model, which was a linear combination of the lamellar and core-shell cylinder model.

The scattering data in this study is plotted on an arbitrary scale. The excess electron densities remained unchanged during the fitting and their values were: $\rho(\text{head group}) = 20 \times 10^{-6}/\text{\AA}^2$ and $\rho(\text{tail}) = 5 \times 10^{-6}/\text{\AA}^2$. Since we used PBS as medium, we set $\rho(\text{solvent}) = 9.4 \times 10^{-6}/\text{\AA}^2$ [59]. These scattering length densities values are relative and can be corrected to match the experimental intensity by the inclusion of a scale factor to the model. Therefore, the parameters being optimized to achieve the best possible fit of the model to the experimental data were: scale factor, head group length, tail length, and cylinder length. Data was fitted by using the LMFIT package [60] for Python.

2.5. Transmission electron microscopy (TEM)

For negative staining TEM; 300 mesh copper grids (EMS, USA), formvar and carbon coated using EM ACE200 (Leica Microsystems, Germany) and glow discharged in PELCO easiGlow (Ted Pella, inc.

USA). 3.5 μl of vesicle solution was adsorbed to the carbon surface for 1 min, washed in two 50 μl drops of water and subsequently stained with 1.5% solution of uranyl acetate (Electron Microscopy Science (EMS), USA), 10 s in three 50 μl drops, blotted to filter paper in between each drop and air-dried. Grids were analyzed with Talos L1200 TEM (FEI, Netherlands, present part of Thermo Fisher Scientific) at 17 500 \times magnification and images recorded with CETA CMOS detector using TIA software (FEI). For cryogenic TEM (cryo-EM) data collection, grids were plunged frozen using the Vitrobot IV (FEI). Holey carbon film coated 300 mesh copper grids (Quantifoil, Germany) were glow discharged. 4 μl vesicles solution was adsorbed for 15 s, blotted for 5 s and plunge frozen into liquid ethane and stored in liquid nitrogen. Grids were loaded by the autoloader system into Titan Krios G2 300 kV TEM (FEI). Images were recorded with K2 BioQuantum, energy filtered direct electron detector using Digital Micrograph software (Gatan, Inc. USA). 33 000 \times magnification resulted in a recorded pixel size of 4.37 \AA . ImageJ (NIH, USA) software were used for vesicle size measurements.

2.6. Computational simulations

Coarse-grain (CG) molecular dynamics (MD) simulations were performed for POPG in presence of different concentrations of LL-

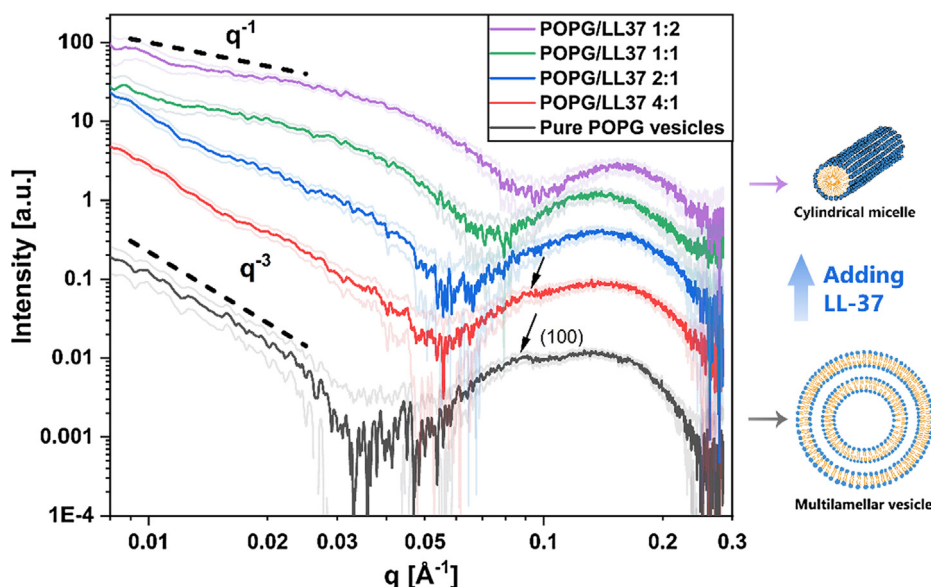


Fig. 1. Colloidal transformations in POPG vesicles upon addition of LL-37 analysed using SAXS. The experimental SAXS profiles with their error bars (transparent lines) represent multilamellar vesicles for pure POPG, with a gradual transition to cylindrical micelles upon addition of LL-37. Dashed lines in the low- q region are calculated with a q^{-3} and q^{-1} power law decay that is characteristic for multilamellar vesicles and cylindrical micelles, as a guide for the eye. The schematics visualise the observed trend in structural transformations upon LL-37 addition to POPG vesicles.

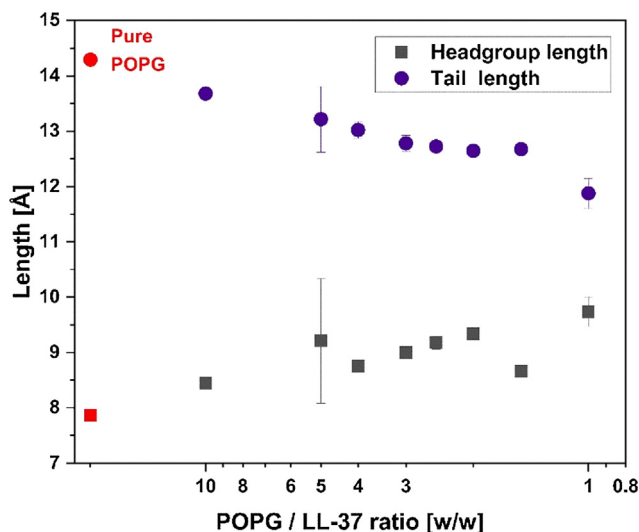


Fig. 2. SAXS model-dependent fitting estimations of the head group and tail length parameters in the vesicles bilayer of POPG systems with increasing LL-37 content.

37 (Table 1) using the MARTINI force field [61,62]. The structure of the LL-37 was built from the atomic coordinates of the antimicrobial peptide obtained via triple-resonance NMR spectroscopy (PDB ID: 2K6O) [63]. The cathelicidin sequence is composed of 37 residues (LLGDF-FRKSK-EKIGK-EFKRI-VQRIK-DFLRN-LVPRT-ES). The atomistic sequence was converted to a coarse-grained representation with generation of the corresponding topology through the Martinize 2.5 python script [64,65]. The initial configurations of

the POPG / LL-37 bilayers were modeled with the N- and C-terminal of LL-37 embedded in the POPG membrane. This bias was applied to facilitate the peptide penetration in the membrane, and the potential formation of pores [66,67].

All systems were solvated with the MARTINI CG water. The full systems were geometry optimized for 5000 steps and simulated under NPT conditions with periodic boundary conditions applied in all directions on each rectangular simulation box. The pressure was kept at 1 bar using the Parrinello-Rahman scheme [68,69], compressibility of $3 \times 10^{-4} \text{ (kJ mol}^{-1} \text{ nm}^{-3})^{-1}$. Two pressure coupling schemes were applied (relaxation time of 12.0 ps), namely semi-isotropic and anisotropic. In the latter regime the compressibility was applied in the xx , yy and zz elements of the matrix. The off-diagonal elements were set to zero to keep a rectangular box. Simulations were run at constant temperature of 300 K by separately coupling the temperatures of the membrane bilayer, peptides and the solvent with a time constant of 1.0 ps using velocity rescaling (v -rescale) with a stochastic term [70]. Following the protocols recommended for the use of MARTINI force field, the non-bonded interactions were cut off at 0.9 nm, using a shift function starting from 1.2 nm for dispersion interactions. The particle-mesh Ewald (PME) [71] was used to calculate the long-range interactions for the atomistic simulations with a Coulomb radius of 1.0 nm, making a grid in the box and checking the atoms in neighboring grid cells every 40 steps. The PME-order was 4 with a Fourier spacing of 0.12 nm. The CG MD simulations were performed using a time-step of 0.03 ps for 3 μ s. Trajectory analyses were performed with GROMACS v. 4.6.7 [71,72] and SuAVE [73] packages. Trajectories and coordinates were visualized using the software VMD v.1.9.3 [74] and systems snapshots were prepared with the *cg_bond* and *cg_helix* scripts from Martini.

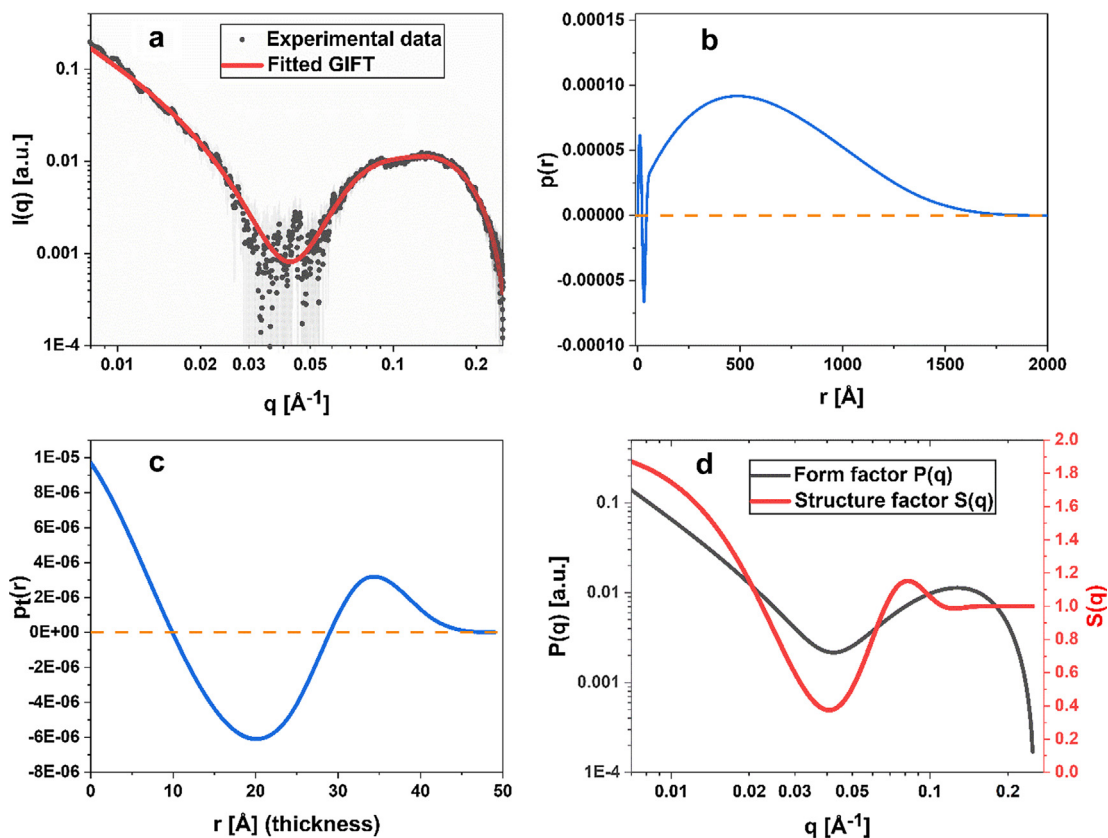


Fig. 3. (a) Experimental SAXS data of the POPG vesicles (symbols) with corresponding fit calculated with the GIFT method (red line) using a multilamellar structure factor; (b) The corresponding $p(r)$ calculated with Eq. (1); (c) The calculated $p(r)$ of the vesicle bilayer thickness; and (d) the corresponding form factor, $P(q)$, and structure factor, $S(q)$, scattering calculated using Eq. (1). (For interpretation of the references to colour in this figure legend, the reader is referred to the web version of this article.)

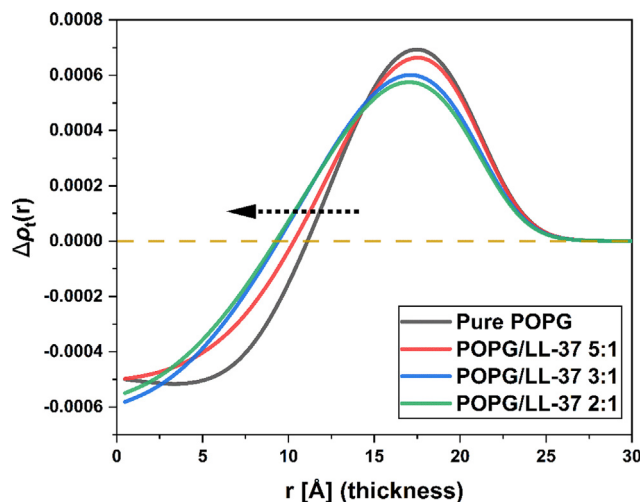


Fig. 4. Excess electron density profile for the half-bilayer calculated from deconvolution of the $p(r)$, using a convolution square-root operation, for POPG vesicles and systems at selected POPG/LL-37 ratios. The corresponding fits to the $p(r)$ are presented in Fig. S2 and S3. The arrow indicates the trend in increasing the head-group - and decreasing the tail volume with increasing content of LL-37.

3. Results and discussion

3.1. Experimental study on POPG/LL-37 self-assembly

The SAXS data of the POPG self-assemblies are characteristic of multilamellar vesicles (MLVs) with a q^{-3} decay of the $I(q)$ at low q values ($q < 0.025 \text{ \AA}^{-1}$), see Fig. 1 [75–77,78]. A broad correlation peak between q around 0.05 \AA^{-1} to 0.3 \AA^{-1} can also be observed that corresponds to the scattering of the lamellar thickness section of the POPG vesicle bilayer. On top of this broad peak, a slightly sharper reflection around q of 0.09 \AA^{-1} is visible, which may arise from the multi-lamellar domains. The weak intensity and broad shape of this peak can be explained by the limited number of bilayer repeat units in the MLVs. Upon addition of increasing amounts of LL-37, this Bragg peak diminishes and the minimum in the scattering profile of POPG at 0.035 \AA^{-1} progressively shifts towards higher q -values, indicating a reduction of the bilayer thickness in the vesicles and increase in the content of single-lamellar vesicles. At POPG/LL-37 mass ratios of 1:1 and 1:2 an approximate q^{-1} dependence of the $I(q)$ in the range between $q = 0.008 \text{ \AA}^{-1}$ and 0.03 \AA^{-1} can be seen that is characteristic for elongated, cylindrical structures (Fig. 1) [79]. In these structures, the broad correlation peak at q between 0.07 \AA^{-1} and 0.3 \AA^{-1} can be attributed to the cross-section of the core-shell type cylindrical micelles.

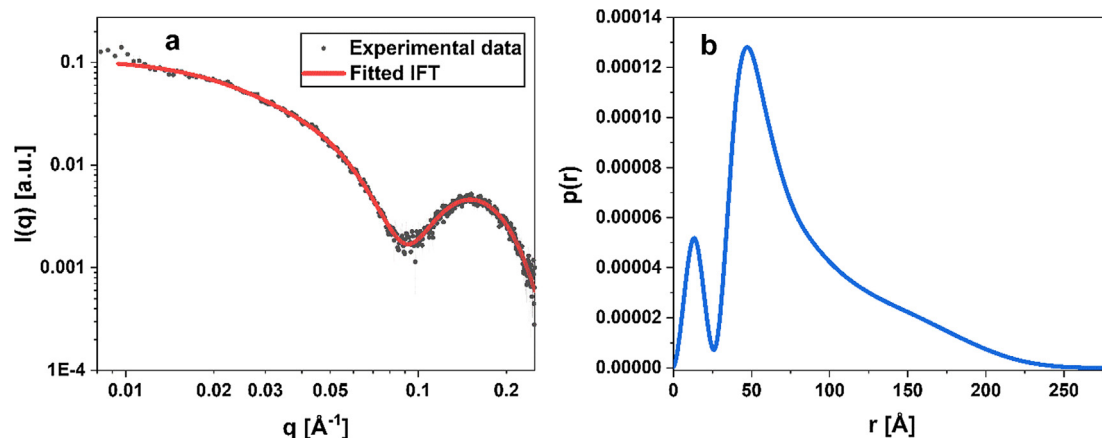


Fig. 5. SAXS analysis of the POPG/LL-37 system at 1:2. (a) Experimental SAXS data (symbols) and fit (red line); (b) The corresponding $p(r)$ from (a) calculated with Eq. (2). (For interpretation of the references to colour in this figure legend, the reader is referred to the web version of this article.)

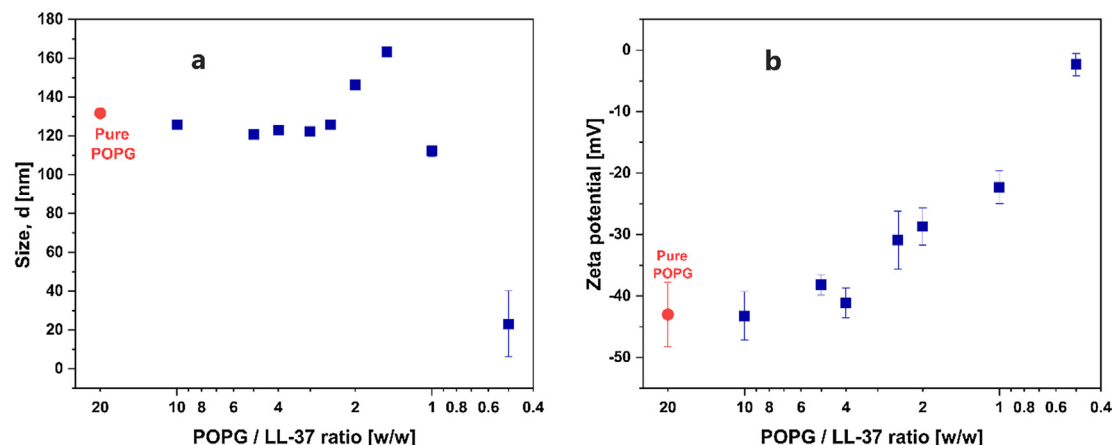


Fig. 6. DLS and zeta potential analysis of the POPG / LL-37 self-assemblies. (a) Dynamic light scattering results on the particle hydrodynamic diameter calculated by the cumulant method; (b) Zeta potential data recorded at selected POPG / LL-37 ratios.

To gain further insights into the structure and morphology of the POPG / LL-37 nano-self-assemblies, a composite model, defined as a linear combination of a form factor model for vesicles (as locally flat bilayer structure) and a form factor model for core-shell cylinders, was used to produce the best possible fit to the experimental SAXS data. Table S1 summarizes the results from the fitting.

The SAXS profile of POPG and POPG/LL-37 of 10:1 could be approximated well with the lamellar model, using Eqs. (4) and (5), as presented in Fig. S1a. Those for systems at higher LL-37 concentration could be satisfactorily approximated with the composite model. Two examples were illustrated: POPG/LL-37 ratio of 3:2 (Fig.S1b) and 1:2 (Fig.S1c). For the POPG vesicles, a bilayer thickness of 42.5 Å was calculated, which is larger than the value of 37 Å found by Kučerka et al. [80]. This difference could arise from the presence of some multilamellar vesicles in our system, and / or the adsorption of counter-ions from the buffer to the bilayer surface, since their experiments were carried out in NaCl solution while ours in PBS.

Upon gradual addition of LL-37 to the POPG vesicles, the apparent size of the head-group gradually increases whereas the tail length decreases (see Eq. (4) and Fig. 2). This result indicates that LL-37 mainly partitions into the lipid-water interface of the bilayers. The SAXS curve at POPG/LL-37 of 2:1 shows a slight upturn at $q < 0.012 \text{ \AA}^{-1}$, which may result from modified structural features during the colloidal transformations of the vesicles. Eventually, a transformation of the vesicles to cylindrical micelles was found at POPG/LL-37 of 1:1. This transformation is in qualitative agreement with predictions from the critical packing parameter (C_{pp}) model [81]. When the effective size of the head group increases, the C_{pp} value will decrease and the lipid molecules will have a preference to self-assemble into structures such as direct cylindrical micelles rather than vesicle bilayers. This modulation of the critical packing parameter by AMPs can be considered as a major mechanism of the antimicrobial effect of such peptides [82].

To further study the dimensions and morphology of the nanoparticles, the $p(r)$ was calculated from the SAXS data using the GIFT method. The shape of the $p(r)$ for POPG self-assemblies (Fig. 3b) is characteristic for vesicles, as reported from theoretical calculations in the literature, where the oscillations at $r < 50 \text{ \AA}$ correspond to the variations in excess electron density within the bilayer region of the vesicles, while the smoother shape of the curve for $r > 50 \text{ \AA}$ corresponds to the general morphology of the vesicle structure.[83] Since the diameter of the vesicles is above the resolution of the SAXS measurements but the GIFT method requires a finite maximum distance, an arbitrary cut-off value of 3000 Å was chosen to mathematically truncate the $p(r)$. Further calculation of the $p_i(r)$ for the POPG bilayers (Fig. 3c) showed the characteristic shape expected for lipid bilayers, confirming the presence of vesicles [84,85]. The negative and positive values in the $p_i(r)$ are caused by the differences in excess electron density between the hydrophilic head group with associated counterions and the hydrophobic alkyl-chain tails of the phospholipids, relative to buffer. The bilayer thickness was estimated around 45 Å from $p_i(r) = 0$, which corresponds well to the result from model-dependent fitting described above. From the calculated multilamellar structure factor model, the number of bilayers was 2.9 ± 0.6 , with a Caillé parameter of 1.2 ± 0.1 . A closer look at the structure factor (Fig. 3d) demonstrates that the deviation from the expected q^{-2} dependence of the $I(q)$ at $q < 0.025 \text{ \AA}^{-1}$ to approximate q^{-3} can be attributed to the structure-factor contribution, together with the very small and broad reflection at q of 0.09 \AA^{-1} that is caused by the spacing between bilayers of around 70 Å (Eq. (3)). The spacing between bilayers is the center-to-center distance between two bilayers within a multilamellar vesicle, including the water layer, and shall not be confused with the bilayer thickness reported above.

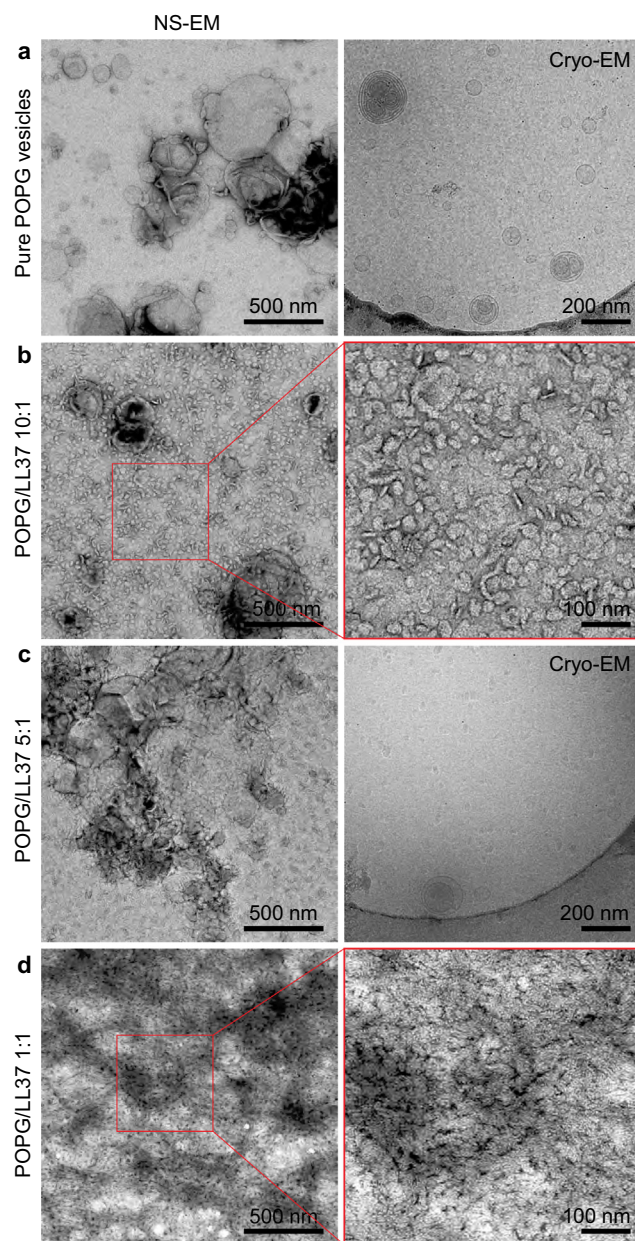


Fig. 7. Negative staining TEM (NS-EM, left column, and cryo-EM images, right column, of the self-assemblies at selected POPG / LL-37 ratios: (a) POPG vesicles; (b) 10:1 ratio; (c) 5:1 ratio and; (d) 1:1 ratio of POPG / LL-37.

The excess electron density profile $\Delta\rho_i(r)$ of the POPG vesicles was calculated for samples with different proportions of LL-37 (Fig. 4) through deconvolution of their respective $p_i(r)$ using a convolution square-root operation (see Fig. S2-3 for corresponding fits). The integration of LL-37 on the lipid vesicle seems to gradually broaden the head group region, while maintaining the overall bilayer thickness. This correlates well with the observations of the model-dependent fitting (Fig. 2) in which the apparent head group size was found to increase while the tail even decreased upon addition of LL-37. This broadening of the excess electron density region of the headgroups indicates that LL-37 interacts more strongly with the polar head group of the POPG rather than its hydrophobic tail. These LL-37 triggered interactions within the bilayer ultimately lead to smaller C_{pp} values and phase transformations into the cylindrical micelles at high enough LL-37 concentrations around POPG/LL-37 of 1:2.

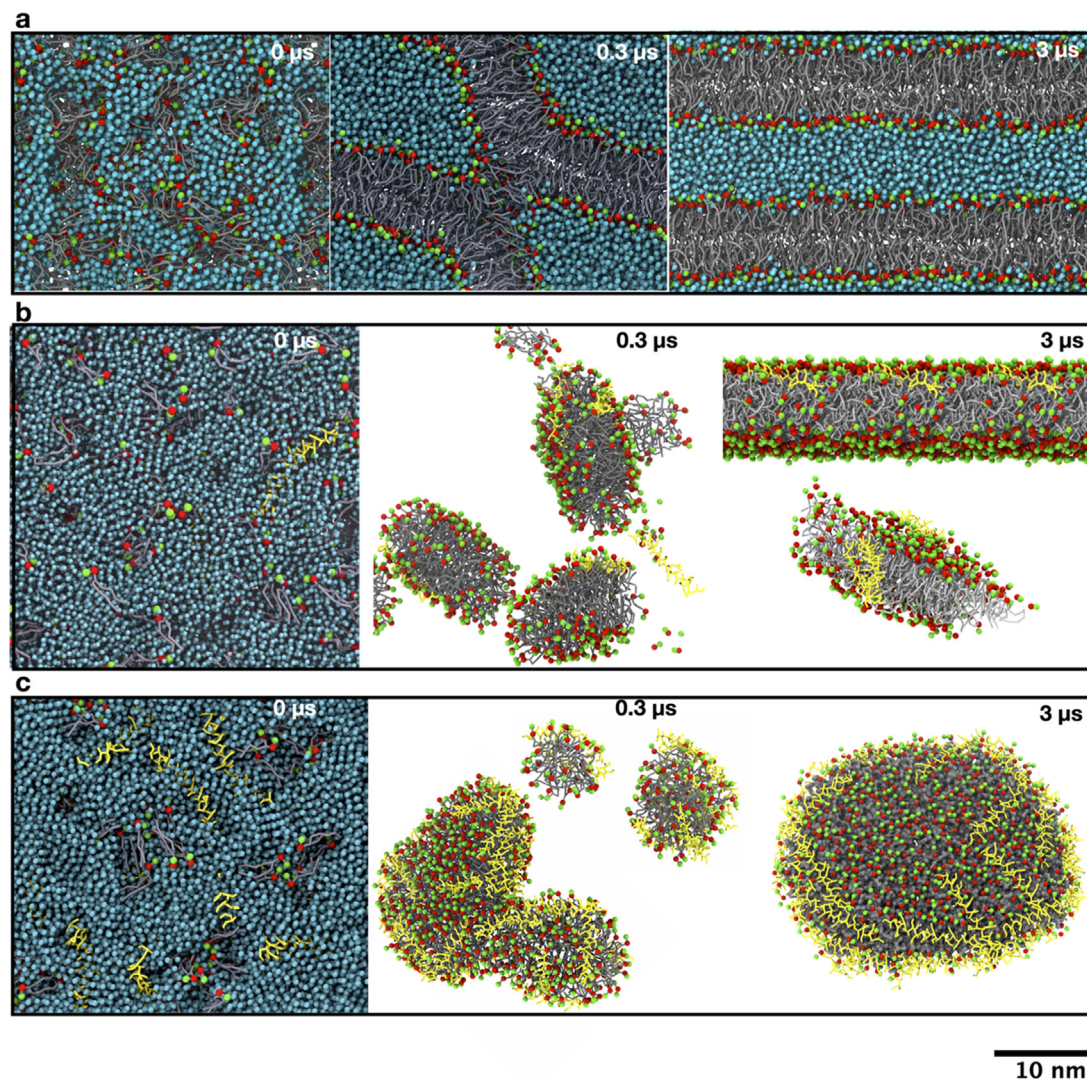


Fig. 8. Time evolution of the self-assembling of aqueous mixtures of (a) pure POPG and POPG / LL-37 ratios of (b) 21:1, (c) 3:1. POPG molecules are represented by red beads (phosphate group), green beads (glycerol group) and grey rods (acyl chains), LL-37 by yellow sticks, and water molecules by light blue beads. Water molecules were not displayed in some of figures to facilitate the visualization of the lipid-protein aggregates. (For interpretation of the references to colour in this figure legend, the reader is referred to the web version of this article.)

The $p(r)$ calculated for the sample POPG/LL-37 at ratio 1:2 (Fig. 5b) shows a shape characteristic of core-shell cylinders [52], in agreement with the result from model-dependent analysis. The length of the cylinder was estimated as 250 Å, which is in agreement with DLS data (Fig. 6). This length is also in agreement with the microscopy images (Fig. 7). In this $p(r)$, the oscillation at $r < \text{around } 50 \text{ Å}$ result from the variation in excess electron density of head and tail groups of the POPG/LL-37 assemblies, while the peak at approximately 50 Å and the gradual decay afterwards correspond to the general morphology of an overall rod-like shape. To gain further insights into the composition of the micelles, the $p_c(r)$ and its correspondent deconvolution were also calculated for this sample (Fig. S4). The cylinder diameter was estimated as 58 Å, which is larger than the estimated bilayer thickness for the POPG vesicles. Such increase could be due to the LL-37 integration at the lipid-water interface.

Dynamic light scattering and zeta potential measurements were used to study the changes in size and charge of the particles (Fig. 6). A hydrodynamic diameter of around 130 nm ($\text{PDI} = 0.28$) was found for the POPG vesicles. Upon addition of LL-37 up to POPG / LL-37 of 1.5:1, the particle size increases up to 163 nm ($\text{PDI} = 0.24$). At POPG/LL-37 of 1:2, the hydrodynamic diameter

abruptly decreases to around 20 nm ($\text{PDI} = 0.21$), in agreement with the SAXS results showing the transition to cylindrical micelles for this sample. The zeta potential measurements (Fig. 6b) show an increase of the potential from -45 mV for the pure POPG vesicles to almost neutral values for the cylindrical micelles at 1:2 POPG/LL-37 ratio. Therefore, the initial increase in particle size (up to 163 nm) upon addition of the peptide may be due to particle aggregation induced by LL-37, which screens the electrical double layer repulsion between the negatively charged POPG particles. This is also in agreement with the indicated aggregation from SAXS data for the sample at POPG/LL-37 of 2:1 as discussed above.

TEM imaging (Fig. 7) of the preparations confirmed the indirect observations from SAXS and DLS. The cryo-EM projection images of plunge frozen hydrated samples show both unilamellar and multilamellar vesicles in the POPG system, supporting the observations of the SAXS scattering curves of the pure POPG self-assemblies. For the systems without LL-37 (Fig. 7a), more than 50% of the vesicles are unilamellar with a diameter below than 50 nm, although larger, multilamellar vesicles were easily spotted. The number of shells on the multilamellar vesicles are mostly smaller than 5, in agreement with the 2.9 ± 0.6 value calculated from the SAXS multilamellar GIFT model. With negative staining TEM imaging, flat-

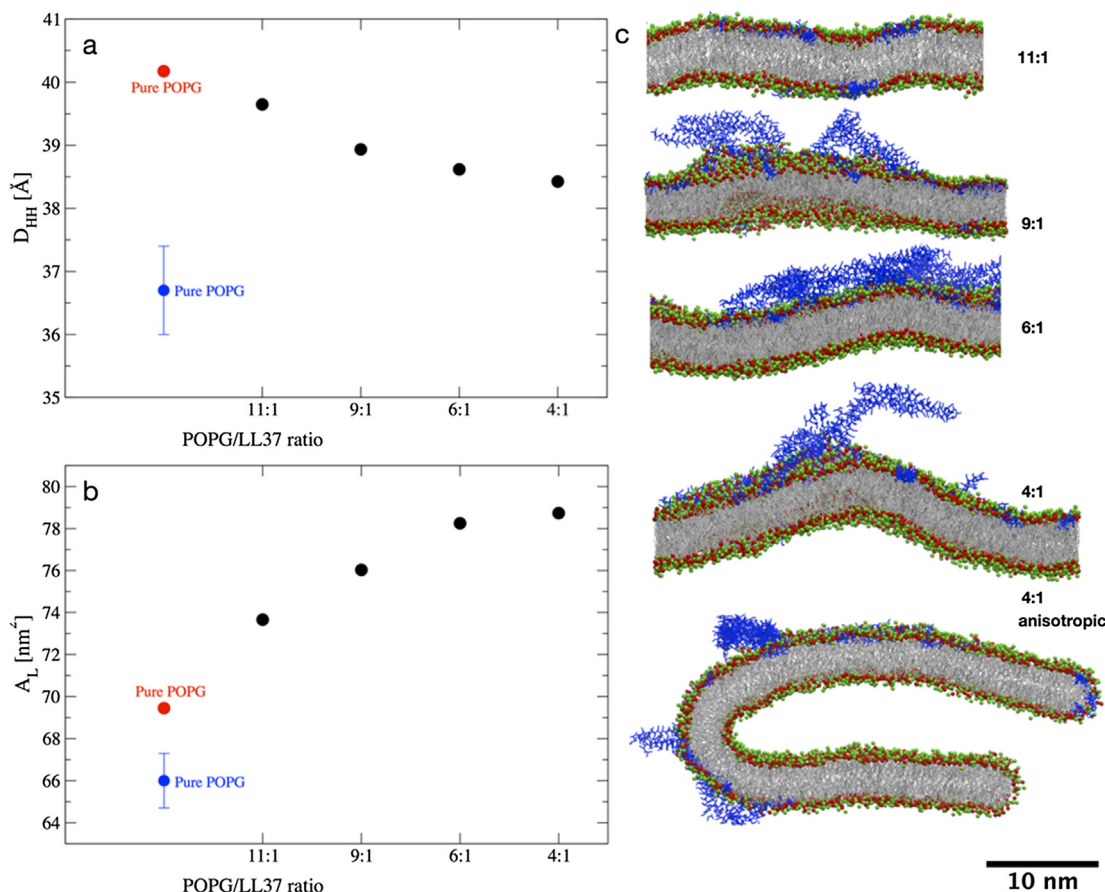


Fig. 9. (a) Membrane thickness (D_{HH}) and (b) Average area per lipid (A_L) from CG simulations of POPG bilayers in the absence and presence of LL37 in different concentrations. Computational and experimental [86] values for pure POPG membranes are shown in red and blue circles. (c) Bilayer arrangement at 3 μ s of CG MD simulations. POPG molecules are represented by red beads (phosphate group), green beads (glycerol group) and grey rods (acyl chains), LL-37 by blue sticks. Water molecules were not displayed for improved clarity. Systems were simulated using semi-isotropic pressure coupling, except for 4:1* which was simulated under anisotropic pressure coupling. (For interpretation of the references to colour in this figure legend, the reader is referred to the web version of this article.)

tened and folded membrane vesicles are observed, most probably dehydrated during the sample preparation. Furthermore, with negative staining TEM imaging of pure POPG, a clean carbon film background indicates that the vast majority of lipid molecules are organized as vesicles. When LL-37 was added to the POPG, a decrease on the number of larger vesicles was observed (Fig. 7b). Also, smaller structures can be seen: disc-like structure with diameter 10–50 nm and rod-like structures with diameter roughly between 5 and 10 nm. TEM reveals that these newly formed structures fill the carbon film background of the sample. As the concentration of LL-37 peptide is increased (Fig. 7c), fewer large vesicles can be seen while the smaller rod and vesicle structures cover more of the background. Finally, at very high LL-37 concentration (Fig. 7d), it is possible to observe curved and possibly branched nanorod-like structures. The high concentration with structures in several layers, hinders the visualisation of these structures. These NS-EM and Cryo-EM images reinforce the considerations from SAXS and DLS in which the POPG self-assemblies shift from vesicles to smaller structures upon addition of LL-37.

3.2. *In silico* study of POPG / LL-37 self-assembly

Further evidence for the partition of LL-37 into the lipid-water interface of the POPG membranes emerges from CG MD simulations with direct implications for the mechanism of action of LL-37 on POPG aggregates (Fig. 8). In all simulated conditions, such as aqueous mixtures and bilayers with different concentrations

of the peptide, LL-37 binds and remains at the lipid-water interface. While simulations of pure POPG in aqueous solution lead to a lamellar arrangement of the phospholipid (Fig. 8a), the addition of LL-37 to the mixture yields a more complex self-assembling pathway which is dependent on POPG/LL-37 mass ratio. The binding of LL-37 to the lipid-water interface increases the effective head group area so that micellar arrangements may be stabilized transiently (POPG/LL-37 mass ratio of 21:1) or persistently (POPG/LL-37 mass ratio of 3:1) (Fig. 8b-c). In the former regime, the amount of LL-37 is not sufficient to increase the effective head group area for micelle formation. Hence, the solvent-exposed hydrophobic surface of small micelles rapidly coalesces into a bilayer which thermodynamically optimizes the distribution of POPG head group and hydrophobic tail in solution (Fig. 8b). Alternately, in the low mass ratio regime (i.e. POPG/LL-37 mass ratio of 3:1), there is formation of small micelles that rapidly coalesce into a larger, very stable, flat micelle which may be referred to as bicelles (Fig. 8c). In this bicelle, the POPG head groups are clustered along the flat polar surface, and LL-37 are distributed around the equatorial edges so that the lipid-water interface is fully covered by hydrophilic chemical entities (Fig. 8c). The bicelle is very stable under the simulated conditions and display an average diameter of ca. 27.7 nm and thickness of 4.4 nm. It should, however, be mentioned that the final dimension of the flat micelle will depend on the total number of lipid molecules used in the simulation box. The number of molecules in the simulated systems is relatively small compared to the experimental setup due to the computa-

tional cost of such calculations. However, the predicted dimensions of these bicelles is compatible with the particle size observations from the dynamic light scattering at highest LL-37 concentration (Fig. 6a) as well as the microscopy images (Fig. 7b–d). As a requirement for the existence of bicelles, lipids at the flatter regions of the bicelle form a bilayer-like arrangement and must have a Cpp close to 1, which would be the case of the POPG molecules, while lipids at the equatorial edges form a micelle-like arrangement and must have a much smaller Cpp, which would correspond to the POPG layers when integrated with LL-37.

MD simulations were also performed for different POPG/LL-37 ratios starting from a semi-isotropic bilayer arrangement which emulates the setup in supported lipid bilayer assays (Table 1). Peptide aggregation/adsorption to the bilayer surface takes place very early in the simulation (<500 ns), and peptide dissociation was not observed within 3 microseconds. Hence, these respective structures are in energy minima from which it can only leave if the system is perturbed. The decrease in POPG/LL-37 mass ratio occurs with a negligible decrease of bilayer thickness (D_{HH}) and increase of the area per lipid (A_L) (Fig. 9). For reference, the largest difference between values of D_{HH} and A_L for the highest and lowest mass ratio simulated is ca. 2 Å and 8 Å², respectively. These differences are near or within the error between measured and calculated values (Fig. 9). Both the SAXS model-dependent (Fig. 2) and the deconvoluted excess electronic density (Fig. 4) analyses agree with the MD simulations on the maintenance of the overall bilayer thickness upon addition of LL-37. During the setup of these systems, the multiple copies of LL-37 were placed with the N- and C-termini embedded in the POPG bilayer. The conformational bias was intended to facilitate the peptide penetration in the bilayer, and the presumed pore formation following previously published protocols [66,67]. However, in all simulated systems LL-37 repositions itself from this initial conformation to bind the lipid-water interface with the longitudinal helical axis oriented parallel to the membrane surface (Fig. 9c). The repositioning occurs faster for simulations at higher POPG/LL-37 mass ratio whereas at higher concentrations of LL-37, some of the peptides are partially in contact with the membrane surface (Fig. 9c), and longer timescales may be required for the complete binding of all peptide molecules. This suggests that the driving force of the LL-37 action lies in the interaction between its positively charged helical face and the negatively charged POPG head groups rather than hydrophobic interactions between the other face of the peptide with the tail of the lipids, in agreement with the observations from SAXS. The MD simulations indicate that LL-37 induces changes in the membrane curvature, which in our simulations occurs above a concentration threshold: In the simulated conditions, the membrane curvature becomes more accentuated above at the 6:1 lipid/peptide ratio, and reaches maximum bending at the 4:1 ratio under anisotropic pressure coupling (Fig. 9c). Such changes in curvature are also in line with the observations from the experimental techniques in this work, supporting the capability of LL-37 to decrease the Cpp of the POPG self-assemblies.

4. Conclusion

The use of AMP delivery systems, or the chemical modification of peptides are valuable options to boost the efficiency and stability of AMPs [87]. Towards the rational design of such novel AMP systems, the mechanism of action of the AMPs underlying the destruction of the bacterial membrane needs to be thoroughly understood. The interaction of membrane-active peptides such as LL-37 with the bacteria membrane was found to depend on a variety of factors including peptide concentration, distribution of charges, hydrophobic groups and environmental parameters [88,89].

In this study, the self-assembly of the AMP LL-37 with bacterial membrane-mimetic POPG vesicles was researched by combining advanced experimental and *in silico* methods. SAXS measurements revealed the progressive transformation of POPG vesicles into smaller self-assembled structures of cylindrical shape at elevated concentrations of the peptide at POPG/LL-37 wt ratio of 1:1 and 1:2. This vesicle to cylindrical micelle transition was also observed with cryo-EM and DLS. DLS results revealed a decrease in the particle diameter from 130 nm (pure POPG vesicles) to around 20 nm upon exposure to increasing amounts of LL-37.

The CG MD simulations provided further molecular insights into the POPG/LL-37 interactions. The main results from the simulations are (i) LL-37 was located at the lipid-water interface; (ii) Increasing the content of LL-37 induced the transition from lamellar to micellar structures via a mechanism of enlargement of the lipid effective headgroup area; and (iii) LL-37 does not appear to spontaneously form pores in pure POPG membranes, but instead induces changes in membrane curvature, ultimately causing the collapse of the vesicle structure. These findings confirm the high capability of LL-37 to influence the self-assembly of lipids and give a direction on the mechanism of action of LL-37 against bacteria in order to enable more rational strategies of fighting the issue of antimicrobial resistance.

Funding Sources

The work was supported by the Swiss National Science Foundation through Project IZBRZ2_186251 and the National Center of Competence in Research Bio-Inspired Materials. Part of this work was performed at Empa in St. Gallen, Switzerland. It further benefitted from support from the Leading House for the Latin America Region, at the Latin-American-Swiss Center (CLS-HSG), University of St. Gallen, Switzerland. The work was partially supported by the Brazilian funding agency FACEPE (APQ-0732-1.06/14). Computational resources were provided by the Swedish National Infrastructure for Computing (SNIC) and the High-Performance Computing Center North (HPC2N). Electron microscopy imaging was supported by SciLifeLab and Swedish research council funding to Umeå Centre for Electron Microscopy (UCEM). The work also benefitted from support from the Swedish Foundation for International Cooperation in Research and Higher Education (STINT, Grant IG2011-2048).

CRediT authorship contribution statement

Rafael V.M. Freire: Investigation, Formal analysis, Visualization, Writing - original draft, Writing - review & editing. **Yeny Pillco-Valencia:** Investigation, Formal analysis, Visualization, Writing - original draft, Writing - review & editing. **Gabriel C.A. Hora:** Investigation, Formal analysis, Visualization, Writing - original draft, Writing - review & editing. **Madeleine Ramstedt:** Conceptualization, Methodology, Investigation, Writing - review & editing. **Linda Sandblad:** Methodology, Investigation, Writing - review & editing. **Thereza A. Soares:** Conceptualization, Methodology, Investigation, Supervision, Writing - review & editing. **Stefan Salentinig:** Conceptualization, Funding acquisition, Project administration, Methodology, Supervision, Investigation, Writing - original draft, Writing - review & editing.

Declaration of Competing Interest

The authors declare that they have no known competing financial interests or personal relationships that could have appeared to influence the work reported in this paper.

Appendix A. Supplementary material

Supplementary data to this article can be found online at <https://doi.org/10.1016/j.jcis.2021.03.060>.

References

- [1] C.A. Michael, D. Dominey-Howes, M. Labbate, The antimicrobial resistance crisis: causes, consequences, and management, *Front Public Health*. 2 (2014) 145, <https://doi.org/10.3389/fpubh.2014.00145>.
- [2] J.M. Ageitos, A. Sanchez-Perez, P. Calo-Mata, T.G. Villa, Antimicrobial peptides (AMPs): ancient compounds that represent novel weapons in the fight against bacteria, *Biochem. Pharmacol.* 133 (2017) 117–138, <https://doi.org/10.1016/j.bcp.2016.09.018>.
- [3] A.K. Marr, W.J. Gooderham, R.E. Hancock, Antibacterial peptides for therapeutic use: obstacles and realistic outlook, *Curr. Opin. Pharmacol.* 6 (2006) 468–472, <https://doi.org/10.1016/j.coph.2006.04.006>.
- [4] A. Rodriguez-Rojas, O. Makarova, J. Rolff, Antimicrobials, stress and mutagenesis, *PLoS Pathog.* 10 (2014), <https://doi.org/10.1371/journal.ppat.1004445> e1004445.
- [5] R.E. Hancock, Rethinking the antibiotic discovery paradigm, *EBioMedicine* 2 (2015) 629–630, <https://doi.org/10.1016/j.ebiom.2015.07.010>.
- [6] A. Lewies, L.H. Du Plessis, J.F. Wentzel, Antimicrobial peptides: the achilles' heel of antibiotic resistance?, *Probiotics Antimicrob. Proteins*. 11 (2019) 370–381, <https://doi.org/10.1007/s12602-018-9465-0>.
- [7] H. Jenssen, P. Hamill, R.E. Hancock, Peptide antimicrobial agents, *Clin Microbiol. Rev.* 19 (2006) 491–511, <https://doi.org/10.1128/CMR.00056-05>.
- [8] F. Schweizer, Cationic amphiphilic peptides with cancer-selective toxicity, *Eur. J. Pharmacol.* 625 (2009) 190–194, <https://doi.org/10.1016/j.ejphar.2009.08.043>.
- [9] D. Gaspar, A.S. Veiga, M.A. Castanho, From antimicrobial to anticancer peptides. A review, *Front Microbiol.* 4 (2013) 294, <https://doi.org/10.3389/fmicb.2013.00294>.
- [10] L.-O. Brandenburg, J. Merres, L.-J. Albrecht, D. Varoga, T. Pufe, Antimicrobial peptides: multifunctional drugs for different applications, *Polymers* 4 (2012) 539–560, <https://doi.org/10.3390/polym4010539>.
- [11] L.J. Otvos, Immunomodulatory effects of anti-microbial peptides, *Acta Microbiol. Immunol. Hung.* 63 (2016) 257–277, <https://doi.org/10.1556/030.63.2016.005>.
- [12] D.S. Alexandre-Ramos, A.E. Silva-Carvalho, M.G. Lacerda, T.R.T. Serejo, O.L. Franco, R.W. Pereira, et al., LL-37 treatment on human peripheral blood mononuclear cells modulates immune response and promotes regulatory T-cells generation, *Biomed. Pharmacother.* 108 (2018) 1584–1590, <https://doi.org/10.1016/j.biopha.2018.10.014>.
- [13] M. Scocchi, M. Mardirossian, G. Runti, M. Benincasa, Non-membrane permeabilizing modes of action of antimicrobial peptides on bacteria, *Curr. Top. Med. Chem.* 16 (2016) 76–88, <https://doi.org/10.2174/1568026615666150703121009>.
- [14] J. Lei, L. Sun, S. Huang, C. Zhu, P. Li, J. He, et al., The antimicrobial peptides and their potential clinical applications, *Am. J. Transl. Res.* 11 (2019) 3919–3931.
- [15] R. Nordstrom, M. Malmsten, Delivery systems for antimicrobial peptides, *Adv. Colloid Interface Sci.* 242 (2017) 17–34, <https://doi.org/10.1016/j.jcis.2017.01.005>.
- [16] R. Innocenti Malini, M. Zabara, M. Gontsarik, K. Maniura-Weber, R.M. Rossi, F. Spano, et al., Self-assembly of glycerol monooleate with the antimicrobial peptide LL-37: a molecular dynamics study, *RSC Adv.* 10 (2020) 8291–8302, <https://doi.org/10.1039/c9ra10037g>.
- [17] U.H. Durr, U.S. Sudheendra, A. Ramamoorthy, LL-37, the only human member of the cathelicidin family of antimicrobial peptides, *Biochim Biophys Acta*. 1758 (2006) 1408–1425, <https://doi.org/10.1016/j.bbame.2006.03.030>.
- [18] G. Wang, X. Li, Z. Wang, APD3: the antimicrobial peptide database as a tool for research and education, *Nucleic Acids Res.* 44 (2016) D1087–D1093, <https://doi.org/10.1093/nar/gkv1278>.
- [19] A.J. Duplantier, M.L. van Hoek, The human cathelicidin antimicrobial peptide LL-37 as a potential treatment for polymicrobial infected wounds, *Front Immunol.* 4 (2013) 143, <https://doi.org/10.3389/fimmu.2013.00143>.
- [20] D.S. Alvares, T.G. Viegas, Neto J. Ruggiero, Lipid-packing perturbation of model membranes by pH-responsive antimicrobial peptides, *Biophys. Rev.* 9 (2017) 669–682, <https://doi.org/10.1007/s12551-017-0296-0>.
- [21] K.A. Henzler Wildman, D.K. Lee, A. Ramamoorthy, Mechanism of lipid bilayer disruption by the human antimicrobial peptide, LL-37, *Biochemistry* 42 (2003) 6545–6558, <https://doi.org/10.1021/bi0273563>.
- [22] G. Wang, B. Mishra, R.F. Eppard, R.M. Eppard, High-quality 3D structures shine light on antibacterial, anti-biofilm and antiviral activities of human cathelicidin LL-37 and its fragments, *Biochim. Biophys. Acta* 1838 (2014) 2160–2172, <https://doi.org/10.1016/j.bbame.2014.01.016>.
- [23] K. Matsuzaki, Control of cell selectivity of antimicrobial peptides, *Biochim. Biophys. Acta*. 1788 (2009) 1687–1692, <https://doi.org/10.1016/j.bbame.2008.09.013>.
- [24] I.S. Tolokh, V. Vivcharuk, B. Tomberli, C.G. Gray, Binding free energy and counterion release for adsorption of the antimicrobial peptide lactoferricin B on a POPC membrane, *Phys. Rev. E Stat. Nonlin. Soft Matter. Phys.* 80 (2009), <https://doi.org/10.1103/PhysRevE.80.031911> 031911.
- [25] M. Manna, C. Mukhopadhyay, Molecular dynamics simulations of the interactions of kinin peptides with an anionic POPG bilayer, *Langmuir* 27 (2011) 3713–3722, <https://doi.org/10.1021/la104046z>.
- [26] B. Ding, L. Soblosky, K. Nguyen, J. Geng, X. Yu, A. Ramamoorthy, et al., Physiologically-relevant modes of membrane interactions by the human antimicrobial peptide, LL-37, revealed by SFG experiments, *Sci. Rep.* 3 (2013) 1854, <https://doi.org/10.1038/srep01854>.
- [27] X. Zhang, K. Oglecka, S. Sandgren, M. Belting, E.K. Esbjornner, B. Norden, et al., Dual functions of the human antimicrobial peptide LL-37-target membrane perturbation and host cell cargo delivery, *Biochim. Biophys. Acta*. 1798 (2010) 2201–2208, <https://doi.org/10.1016/j.bbame.2009.12.011>.
- [28] L. Zhao, Z. Cao, Y. Bian, G. Hu, J. Wang, Y. Zhou, Molecular dynamics simulations of human antimicrobial peptide LL-37 in model POPC and POPG lipid bilayers, *Int. J. Mol. Sci.* 19 (2018), <https://doi.org/10.3390/ijms19041186>.
- [29] E.F. Haney, S. Nathoo, H.J. Vogel, E.J. Prenner, Induction of non-lamellar lipid phases by antimicrobial peptides: a potential link to mode of action, *Chem. Phys. Lipids*. 163 (2010) 82–93, <https://doi.org/10.1016/j.chemphyslip.2009.09.002>.
- [30] A. Hickel, S. Danner-Pongratz, H. Amenitsch, G. Degovics, M. Rappolt, K. Lohner, et al., Influence of antimicrobial peptides on the formation of nonlamellar lipid mesophases, *Biochim. Biophys. Acta*. 1778 (2008) 2325–2333, <https://doi.org/10.1016/j.bbame.2008.05.014>.
- [31] K. Kornmueller, B. Lehofer, G. Leitinger, H. Amenitsch, R. Prassl, Peptide self-assembly into lamellar phases and the formation of lipid-peptide nanostructures, *Nano Res.* 11 (2018) 913–928, <https://doi.org/10.1007/s12274-017-1702-4>.
- [32] E. Sevcik, G. Pabst, W. Richter, S. Danner, H. Amenitsch, K. Lohner, Interaction of LL-37 with model membrane systems of different complexity: influence of the lipid matrix, *Biophys. J.* 94 (2008) 4688–4699, <https://doi.org/10.1529/biophysj.107.123620>.
- [33] D. Ciunac, H. Gong, X. Hu, J.R. Lu, Membrane targeting cationic antimicrobial peptides, *J. Colloid Interface Sci.* 537 (2019) 163–185, <https://doi.org/10.1016/j.jcis.2018.10.103>.
- [34] F. Morgera, L. Vaccari, N. Antcheva, D. Scaini, S. Pacor, A. Tossi, Primate cathelicidin orthologues display different structures and membrane interactions, *Biochem. J.* 417 (2009) 727–735, <https://doi.org/10.1042/BJ20081726>.
- [35] C.C. Lee, Y. Sun, S. Qian, H.W. Huang, Transmembrane pores formed by human antimicrobial peptide LL-37, *Biophys. J.* 100 (2011) 1688–1696, <https://doi.org/10.1016/j.bpj.2011.02.018>.
- [36] D. Khindoli, S. Pacor, F. Guida, N. Antcheva, A. Tossi, Native oligomerization determines the mode of action and biological activities of human cathelicidin LL-37, *Biochem. J.* 457 (2014) 263–275, <https://doi.org/10.1042/BJ20131048>.
- [37] Z. Oren, J.C. Lerman, G.H. Gudmundsson, B. Agerberth, Y. Shai, Structure and organization of the human antimicrobial peptide LL-37 in phospholipid membranes: relevance to the molecular basis for its non-cell-selective activity, *Biochem. J.* 341 (1999) 501–513, <https://doi.org/10.1042/bj3410501>.
- [38] F. Neville, M. Cahuzac, O. Kononov, Y. Ishitsuka, K.Y. Lee, I. Kuzmenko, et al., Lipid headgroup discrimination by antimicrobial peptide LL-37: insight into mechanism of action, *Biophys. J.* 90 (2006) 1275–1287, <https://doi.org/10.1529/biophysj.105.067595>.
- [39] F. Porcelli, R. Verardi, L. Shi, K.A. Henzler-Wildman, A. Ramamoorthy, G. Veglia, NMR structure of the cathelicidin-derived human antimicrobial peptide LL-37 in dodecylphosphocholine micelles, *Biochemistry* 47 (2008) 5565–5572, <https://doi.org/10.1021/bi702036s>.
- [40] Catalina A de Miguel, E. Forbrig, J. Kozuch, C. Nehls, L. Paulowski, T. Gutschmann, et al., The C-terminal VPRTS Tail of LL-37 influences the mode of attachment to a lipid bilayer and antimicrobial activity, *Biochemistry* 58 (2019) 2447–2462, <https://doi.org/10.1021/acs.biochem.8b01297>.
- [41] E. Sancho-Vaello, P. Francois, E.J. Bonetti, L. Lilie, S. Finger, F. Gil-Ortiz, et al., Structural remodeling and oligomerization of human cathelicidin on membranes suggest fibril-like structures as active species, *Sci. Rep.*. 7 (2017) 15371, <https://doi.org/10.1038/s41598-017-14206-1>.
- [42] J.E. Nielsen, V.A. Bjornestad, V. Pipich, H. Jenssen, R. Lund, Beyond structural models for the mode of action: how natural antimicrobial peptides affect lipid transport, *J. Colloid Interface Sci.* 582 (2021) 793–802, <https://doi.org/10.1016/j.jcis.2020.08.094>.
- [43] T.G. Meikle, A. Zabara, L.J. Waddington, F. Separovic, C.J. Drummond, C.E. Conn, Incorporation of antimicrobial peptides in nanostructured lipid membrane mimetic bilayer cubosomes, *Colloids Surf. B Biointerfaces*. 152 (2017) 143–151, <https://doi.org/10.1016/j.colsurfb.2017.01.004>.
- [44] T.G. Meikle, C.E. Conn, F. Separovic, C.J. Drummond, Exploring the structural relationship between encapsulated antimicrobial peptides and the bilayer membrane mimetic lipidic cubic phase: studies with gramicidin A', *RSC Adv.* 6 (2016) 68685–68694, <https://doi.org/10.1039/c6ra13658c>.
- [45] M. Gontsarik, M.T. Buhmann, A. Yagmur, Q. Ren, K. Maniura-Weber, S. Salentini, Antimicrobial peptide-driven colloidal transformations in liquid-crystalline nanocarriers, *J. Phys. Chem. Lett.* 7 (2016) 3482–3486, <https://doi.org/10.1021/acs.jpclett.6b01622>.
- [46] M. Zabara, B. Senturk, M. Gontsarik, Q. Ren, M. Rottmar, K. Maniura-Weber, et al., Multifunctional nano-biointerfaces: cyto-compatible antimicrobial nanocarriers from stabilizer-free cubosomes, *Adv. Funct. Mater.* 29 (2019), <https://doi.org/10.1002/adfm.201904007>.
- [47] M. Gontsarik, M. Mohammadtaheri, A. Yagmur, S. Salentini, pH-Triggered nanostructural transformations in antimicrobial peptide/oleic acid self-

- assemblies, *Biomater. Sci.* 6 (2018) 803–812, <https://doi.org/10.1039/c7bm00929a>.
- [48] M. Gontsarik, A. Yagmur, Q. Ren, K. Maniura-Weber, S. Salentinig, From structure to function: pH-switchable antimicrobial nano-self-assemblies, *ACS Appl Mater Interfaces*. 11 (2019) 2821–2829, <https://doi.org/10.1021/acami.8b18618>.
- [49] Pecora R. *Dynamic Light Scattering*. New York: Plenum Press; 1985. DOI 10.1007/978-1-4613-2389-1.
- [50] D.E. Koppel, Analysis of macromolecular polydispersity in intensity correlation spectroscopy: the method of cumulants, *J. Chem. Phys.* 57 (1972) 4814–4820, <https://doi.org/10.1063/1.1678153>.
- [51] P.W. Schmidt, Interpretation of small-angle scattering curves proportional to a negative power of the scattering vector, *J. Appl. Crystallogr.* 15 (1982) 567–569, <https://doi.org/10.1107/s002188988201259x>.
- [52] J. Brunner-Popela, O. Glatter, Small-angle scattering of interacting particles. I. Basic principles of a global evaluation technique, *J. Appl. Crystallogr.* 30 (1997) 431–442, <https://doi.org/10.1107/s0021889896015749>.
- [53] T. Fröhlich, G. Fritz, N. Freiberg, O. Glatter, Structure and order in lamellar phases determined by small-angle scattering, *J. Appl. Crystallogr.* 37 (2004) 703–710, <https://doi.org/10.1107/s0021889804012956>.
- [54] A. Bergmann, G. Fritz, O. Glatter, Solving the generalized indirect Fourier transformation (GIFT) by Boltzmann simplex simulated annealing (BSSA), *J. Appl. Crystallogr.* 33 (2000) 1212–1216, <https://doi.org/10.1107/s0021889800008372>.
- [55] O. Glatter, Convolution square root of band-limited symmetrical functions and its application to small-angle scattering data, *J. Appl. Crystallogr.* 14 (1981) 101–108, <https://doi.org/10.1107/s002188988100887x>.
- [56] O. Glatter, Evaluation of small-angle scattering data from lamellar and cylindrical particles by the indirect transformation method, *J. Appl. Crystallogr.* 13 (1980) 577–584, <https://doi.org/10.1107/s0021889880012794>.
- [57] F. Nallet, R. Laversanne, D. Roux, Modelling X-ray or neutron scattering spectra of lyotropic lamellar phases: interplay between form and structure factors, *J. Phys. II* (3) (1993) 487–502, <https://doi.org/10.1051/jp2:1993146>.
- [58] Livsey I. Neutron scattering from concentric cylinders. Intraparticle interference function and radius of gyration. *Journal of the Chemical Society, Faraday Transactions 2*. 1987;83. DOI 10.1039/f29878301445.
- [59] C.H. Yang, T.L. Lin, U.S. Jeng, Small-angle X-ray scattering studies on the structure of disc-shaped bicelles incorporated with neutral PEGylated lipids, *Langmuir* 35 (2019) 9483–9492, <https://doi.org/10.1021/acs.langmuir.9b00756>.
- [60] M. Newville, T. Stensitzki, D.B. Allen, A. Ingargiola, LMFIT: non-linear least-square minimization and curve-fitting for python, Zenodo. (2014), <https://doi.org/10.5281/zenodo.11813>.
- [61] L. Monticelli, S.K. Kandasamy, X. Periole, R.G. Larson, D.P. Tieleman, S.J. Marrink, The MARTINI coarse-grained force field: extension to proteins, *J. Chem. Theory Comput.* 4 (2008) 819–834, <https://doi.org/10.1021/ct700324x>.
- [62] S.J. Marrink, H.J. Risselada, S. Yefimov, D.P. Tieleman, A.H. de Vries, The MARTINI force field: coarse grained model for biomolecular simulations, *J. Phys. Chem. B* 111 (2007) 7812–7824, <https://doi.org/10.1021/jp071097f>.
- [63] G. Wang, Structures of human host defense cathelicidin LL-37 and its smallest antimicrobial peptide KR-12 in lipid micelles, *J. Biol. Chem.* 283 (2008) 32637–32643, <https://doi.org/10.1074/jbc.M805533200>.
- [64] D.H. de Jong, G. Singh, W.F. Bennett, C. Arnarez, T.A. Wassenaar, L.V. Schafer, et al., Improved parameters for the martini coarse-grained protein force field, *J. Chem. Theory Comput.* 9 (2013) 687–697, <https://doi.org/10.1021/ct300646g>.
- [65] Martini Forcefield webpage: <http://www.cgmartini.nl/index.php>.
- [66] E.N. Lorenzon, T.M. Nobre, L. Caseli, E.M. Cilli, G.C.A. da Hora, T.A. Soares, et al., The “pre-assembled state” of magainin 2 lysine-linked dimer determines its enhanced antimicrobial activity, *Colloids Surf B Biointerfaces*. 167 (2018) 432–440, <https://doi.org/10.1016/j.colsurfb.2018.04.034>.
- [67] K.P. Santo, M.L. Berkowitz, Difference between magainin-2 and melittin assemblies in phosphatidylcholine bilayers: results from coarse-grained simulations, *J. Phys. Chem. B* 116 (2012) 3021–3030, <https://doi.org/10.1021/jp212018f>.
- [68] M. Parrinello, A. Rahman, Polymorphic transitions in single crystals: a new molecular dynamics method, *J. Appl. Phys.* 52 (1981) 7182–7190, <https://doi.org/10.1063/1.328693>.
- [69] S. Nosé, M.L. Klein, Constant pressure molecular dynamics for molecular systems, *Mol. Phys.* 50 (2006) 1055–1076, <https://doi.org/10.1080/00268978300102851>.
- [70] G. Bussi, D. Donadio, M. Parrinello, Canonical sampling through velocity rescaling, *J. Chem. Phys.* 126 (2007), <https://doi.org/10.1063/1.2408420>.
- [71] B. Hess, C. Kutzner, D. van der Spoel, E. Lindahl, GROMACS 4: algorithms for highly efficient, load-balanced, and scalable molecular simulation, *J. Chem. Theory Comput.* 4 (2008) 435–447, <https://doi.org/10.1021/ct700301q>.
- [72] D. Van Der Spoel, E. Lindahl, B. Hess, G. Groenhof, A.E. Mark, H.J. Berendsen, GROMACS: fast, flexible, and free, *J. Comput. Chem.* 26 (2005) 1701–1718, <https://doi.org/10.1002/jcc.20291>.
- [73] D.E.S. Santos, F.J.S. Pontes, R.D. Lins, K. Coutinho, T.A. Soares, SuAVE: a tool for analyzing curvature-dependent properties in chemical interfaces, *J. Chem. Inf. Model.* 60 (2020) 473–484, <https://doi.org/10.1021/acs.jcim.9b00569>.
- [74] W. Humphrey, A. Dalke, K. Schulten, VMD: visual molecular dynamics, *J. Mol. Graph.* 14 (1996) 33–38, [https://doi.org/10.1016/0263-7855\(96\)00018-5](https://doi.org/10.1016/0263-7855(96)00018-5).
- [75] K. Komorowski, A. Salditt, Y. Xu, H. Yavuz, M. Brennich, R. Jahn, et al., Vesicle adhesion and fusion studied by small-angle X-ray scattering, *Biophys. J.* 114 (2018) 1908–1920, <https://doi.org/10.1016/j.bpj.2018.02.040>.
- [76] M.R. Brzustowicz, A.T. Brunger, X-ray scattering from unilamellar lipid vesicles, *J. Appl. Crystallogr.* 38 (2005) 126–131, <https://doi.org/10.1107/s0021889804029206>.
- [77] Narayanan T, Gummel J, Gradzielski M. Probing the Self-Assembly of Unilamellar Vesicles Using Time-Resolved SAXS. In: Iglíč A, Kulkarni CV, editors. *Advances in Planar Lipid Bilayers and Liposomes*; Elsevier; 2014. p. 171–96. DOI 10.1016/b978-0-12-418698-9.00007-1.
- [78] H. Frielinghaus, Small-angle scattering model for multilamellar vesicles, *Phys. Rev. E Stat. Nonlin. Soft Matter. Phys.* 76 (2007), <https://doi.org/10.1103/PhysRevE.76.051603>.
- [79] G. Ochbaum, R. Bittou. Using small-angle X-ray scattering (SAXS) to study the structure of self-assembling biomaterials. In: Azevedo HS, da Silva RMP, editors. *Self-assembling Biomaterials: Molecular Design, Characterization and Application in Biology and Medicine*. Cambridge, UK: Woodhead Publishing; 2018. p. 291–304. DOI 10.1016/B978-0-08-102015-9.00015-0.
- [80] N. Kucerka, B.W. Holland, C.G. Gray, B. Tomberli, J. Katsaras, Scattering density profile model of POPG bilayers as determined by molecular dynamics simulations and small-angle neutron and X-ray scattering experiments, *J. Phys. Chem. B* 116 (2012) 232–239, <https://doi.org/10.1021/jp208920h>.
- [81] D. Lombardo, M.A. Kiselev, S. Magazú, P. Calandra, Amphiphiles self-assembly: basic concepts and future perspectives of supramolecular approaches, *Adv. Condens. Matter Phys.* 2015 (2015) 1–22, <https://doi.org/10.1155/2015/151683>.
- [82] D. Koller, K. Lohner, The role of spontaneous lipid curvature in the interaction of interfacially active peptides with membranes, *Biochim. Biophys. Acta*. 1838 (2014) 2250–2259, <https://doi.org/10.1016/j.bbammem.2014.05.013>.
- [83] R. Sreij, C. Dargel, R. Schweins, S. Prevost, R. Dattani, T. Hellweg, Aescin-cholesterol complexes in DMPC Model membranes: A DSC and temperature-dependent scattering study, *Sci. Rep.* 9 (2019) 5542, <https://doi.org/10.1038/s41598-019-41865-z>.
- [84] S. Šegota, Đ. Težak, Y. Talmon, New catanionic mixtures of didodecyltrimethylammonium bromide/sodium dodecylbenzene sulfonate/water with special reference to spontaneous formation of vesicles. II. Size and shape analysis by SAXS, light scattering, Cryo-TEM, and light microscopy, *Soft Mater.* 3 (2006) 51–69, <https://doi.org/10.1080/15394450600683477>.
- [85] S. Salentinig, L. Sagalowicz, M.E. Leser, C. Tedeschi, O. Glatter, Transitions in the internal structure of lipid droplets during fat digestion, *Soft Matter* 7 (2011) 650–661, <https://doi.org/10.1039/c0sm00491j>.
- [86] J. Pan, F.A. Heberle, S. Tristram-Nagle, M. Szymanski, M. Koepfinger, J. Katsaras, et al., Molecular structures of fluid phase phosphatidylglycerol bilayers as determined by small angle neutron and X-ray scattering, *Biochim Biophys Acta*. 1818 (2012) 2135–2148, <https://doi.org/10.1016/j.bbammem.2012.05.007>.
- [87] M. Divyashree, M.K. Mani, D. Reddy, R. Kumavath, P. Ghosh, V. Azevedo, et al., Clinical applications of antimicrobial peptides (AMPs): where do we stand now?, *Protein Pept. Lett.* 27 (2020) 120–134, <https://doi.org/10.2174/0929866526666190925152957>.
- [88] C.H. Chen, T.K. Lu, Development and challenges of antimicrobial peptides for therapeutic applications, *Antibiotics (Basel)* 9 (2020), <https://doi.org/10.3390/antibiotics9010024>.
- [89] M. Mahlapuu, C. Björn, J. Ekblom, Antimicrobial peptides as therapeutic agents: opportunities and challenges, *Crit. Rev. Biotechnol.* 40 (2020) 978–992, <https://doi.org/10.1080/07388551.2020.1796576>.